PHYSICAL REVIEW E **100**, 022602 (2019)

Hexagonal deposits of colloidal particles

Hee Kyeong Park,[1,2,*] Yeseul Kim,[1,2,*] Hyeongho Min,[3] Changhyun Pang,[3] and Byung Mook Weon[1,2,†]
[1]*Soft Matter Physics Laboratory, School of Advanced Materials Science and Engineering,*
SKKU Advanced Institute of Nanotechnology (SAINT), Sungkyunkwan University, Suwon 16419, South Korea
[2]*Research Center for Advanced Materials Technology, Sungkyunkwan University, Suwon 16419, South Korea*
[3]*Department of Chemical Engineering, SKKU Advanced Institute of Nanotechnology (SAINT),*
Sungkyunkwan University, Suwon 16419, South Korea

(Received 19 April 2019; published 6 August 2019)

Colloidal particles are essential materials for modern inkjet printing and coating. Here we demonstrate a versatile method to achieve hexagonal deposits of colloidal particles through droplet evaporation on hexagonal micropillar arrays. We identify how colloidal fluids turn into hexagonal deposits during evaporation with x-ray tomography. Interestingly, evaporation-driven hexagonal deposits are quite crack-free uniform. We attribute hexagonal deposit shape control to local contact line pinning by colloidal particles and geometric constraints by micropillar arrays. This deposition strategy offers a feasibility for high-quality evaporation-driven crack-free uniform polygonal deposits of colloidal particles for diverse applications.

DOI: 10.1103/PhysRevE.100.022602

I. INTRODUCTION

Colloidal fluids include various kinds of solvents and soluble solutes or insoluble colloids or colloidal nanoparticles [1]. Colloidal particles are promising ingredients for modern inkjet printing and coating technologies mostly thanks to economical advantage of evaporation processes [2–6]. Modern technologies that utilize colloidal fluids require crack-free uniform deposits for advanced applications into printed electronics and biomedical devices [6,7]. Indeed, droplet evaporation is a phase transition regarding three phases of solid, liquid, and air [8–10], so that intrinsic complexity exists in manipulating droplet evaporation. Particularly, droplet evaporation may induce crack formation [11] and nonuniform deposition (the coffee-ring effect) of colloidal nanoparticles [12–15]. Achieving crack-free uniform deposition of colloids is a difficult task because of complexity in droplet evaporation of colloidal fluids [16,17]. Interestingly, noncircular wetting patterns of liquid droplets on lithographically patterned surfaces enable fabrication of polygonal droplets during evaporation [18–20]. Despite extensive studies on deposits of colloidal particles from colloidal fluids [21–24], there is no report to achieve polygonal deposits of colloidal particles on micropatterned surfaces through droplet evaporation.

In this letter, we demonstrate a feasible method to achieve hexagonal deposits of colloidal particles through well-controlled droplet evaporation of colloidal fluids on hexagonal micropillar arrays. Using high-speed high-resolution x-ray tomography, we show how colloidal fluids on micropillar arrays evaporate and spread through micropillars and eventually turn into hexagonal deposits. Interestingly, evaporation-driven hexagonal deposits are quite crack-free uniform. We discuss a possible mechanism of deposit shape control with local contact line pinning by colloidal particles and modify a previous explanation for droplet shape control of pure fluids by micropillars [18–20]. This work incorporates two ideas for droplet shape control on micropatterned surfaces [18–20] and drying-mediated colloidal assembly [21–24], which are relevant to wettability and evaporation on rough surfaces [25–28]. This deposition strategy would contribute to high-quality evaporation-driven crack-free uniform polygonal deposits of colloidal particles for applications into modern inkjet printing for printed electronics and nanoparticle self-assembly or biomedical fabrication for DNA microarray and cost-effective disease identification [29–32].

II. EXPERIMENTAL PROCEDURE

A. Colloidal fluids and micropillar arrays

In experiments, we used aqueous colloidal suspensions that contain 2.5 ± 0.1 vol.% monodispersed polystyrene particles for diameters $d = 0.1$ μm, 0.5 μm, 1.0 μm, 10 μm, and 20 μm, purchased from Polyscience Inc (Warrington, North America). Cylindrical polydimethylsiloxane micropillar arrays arranged in hexagonal patterns were fabricated by soft lithography and subsequent etching process [33]. Particularly, to control micropillar geometry, pillar pitch (P) was changed as 30, 90, 120, and 140 μm under fixed conditions of pillar diameter (D) and height (H) as 30 and 100 μm, respectively. A representative hexagonal micropillar array was taken by scanning electron microscopy (SEM) as demonstrated in Fig. 1(a). SEM analysis (S-3000H, Hitachi) was employed to provide additional microscopic information for micropillar arrays and hexagonal deposits. Small volume droplets from colloidal suspensions with fixed initial volumes of 2.0 ± 0.2 μl were generated by using a micropipette. Each droplet was gently placed on micropillar surfaces and all

---

[*] H.K.P. and Y.K. contributed equally to this work.

[†] bmweon@skku.edu

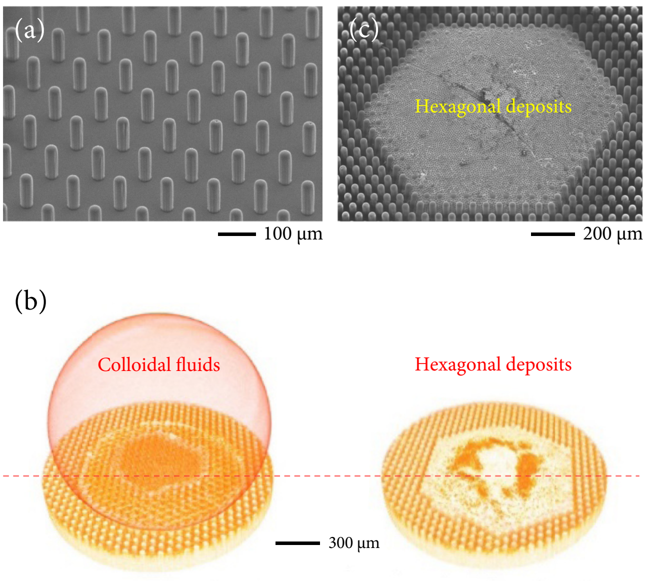

FIG. 1. Hexagonal deposits. (a) A scanning electron microscopy (SEM) image of hexagonal micropillar arrays. (b) Reconstructed x-ray tomography images of colloidal fluids on hexagonal micropillar arrays (left) and hexagonal deposits after evaporation (right). (c) A representative SEM image of reproducible hexagonal deposits on hexagonal micropillar arrays. Here, hexagonal deposits of colloidal particles are quite crack-free uniform.

evaporation experiments were conducted at room temperature and humidity (temperature $= 24\,^{\circ}\mathrm{C}$, humidity $= 30\%$).

B. X-ray tomography of evaporation dynamics

We simply put colloidal droplets on hexagonal micropillar arrays and eventually obtained hexagonal deposits through droplet evaporation. To understand how hexagonal deposits remain during evaporation, we observed *in situ* two-dimensional (2D) and 3D evaporation dynamics with high-speed high-resolution x-ray tomography during evaporation. A full tomography dataset for an evaporating drop was acquired in 7 s which enables to *in situ* 2D and 3D microscopic observations. X-ray imaging experiments were conducted in the 6C Bio Medical Imaging beamline established at the Pohang Light Source (PLS-II) that provided monochromatic synchrotron x-rays with 24-keV energy and a $1.4 \times 1.7\ \mathrm{mm}^2$ beam size. After penetrating samples, x-rays were converted into visible lights by the scintillator (LuAG:Ce 50 μm) and corrected by the Scientific Complementary Metal-Oxide-Semiconductor (sCMOS) camera (Andor Zyla) with magnification of 10×. The minimum pixel size was approximately 0.66 μm, and the field of view was $1.70 \times 1.40\ \mathrm{mm}^2$. As examples, reconstructed 3D images taken from x-ray tomography of colloidal fluids and hexagonal deposits are illustrated in Fig. 1(b). Microscopic 3D images of evaporating colloidal fluids were reproduced by stacking reconstructed slices vertically. Three-dimensional image visualization with image processing and analysis was achieved by Amira as a commercial software (FEI, Hillsboro, Oregon). After droplet evaporation of colloidal fluids, quite crack-free uniform hexagonal deposits remain inside micropillar hexagonal arrays as demonstrated in Fig. 1(c) taken by SEM. Additionally, a digital microscope (VH-Z100R, Keyence) was used to visualize temporal evolution of droplet contact line motion. Measurements of droplet contact angle and diameter were recorded at 1 s intervals by using a drop shape analyzer (DSA25 and KRUSS).

III. RESULTS AND DISCUSSION

A. Three distinct evaporation deposits

We find three distinct kinds of evaporation-driven colloidal deposits: hexagonal deposits, Wenzel deposits, and Cassie-Baxter deposits, as demonstrated by reconstructed 3D images taken from x-ray tomography in Fig. 2. Here 3D temporal sequential images for droplet evaporation show that colloidal droplets on hexagonal micropillar arrays gradually evaporate and eventually remain in three different deposits. Two evaporation processes regarding Wenzel and Cassie-Baxter deposits are quite comprehensible immediately from Wenzel and Cassie-Baxter wetting transitions on rough surfaces [8,34–37]. However, why hexagonal deposits remain need to be explained. In this study, the most important central question is how geometric constraints such as droplet size, micropillary array, and colloidal particle size determine evaporation-driven hexagonal deposits.

B. Evaporation dynamics for hexagonal deposits

We investigate the evaporation process for hexagonal deposits in top and side views taken from 3D x-ray tomography as illustrated in Figs. 3(a) and 3(b). Three-dimensional temporal sequential microscopic observations for hexagonal deposits at $t/t_f > 0.90$ (where t_f is the complete evaporation time) show that circular bottoms at $t/t_f \sim 0.90$ rapidly

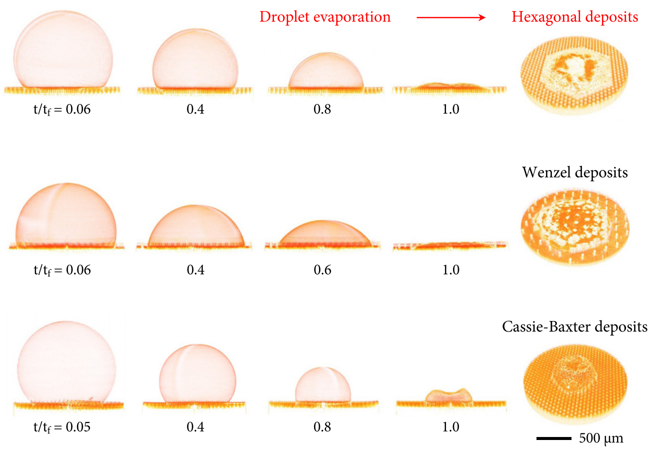

FIG. 2. Three different colloidal deposits. As marked, hexagonal deposits (upper), Wenzel deposits (middle), and Cassie-Baxter deposits (lower) were driven by droplet evaporation. Such different colloidal deposits would be constrained by geometric conditions regarding droplet size, micropillar geometry, and particle size. Here hexagonal deposits appear at $L = 60\ \mu$m, $D = 30\ \mu$m, $d = 10\ \mu$m, Wenzel deposits at $L = 170\ \mu$m, $D = 30\ \mu$m, $d = 10\ \mu$m, and Cassie-Baxter deposits at $L = 60\ \mu$m, $D = 30\ \mu$m, $d = 1.0\ \mu$m. All images were reconstructed from *in situ* 3D x-ray tomography.

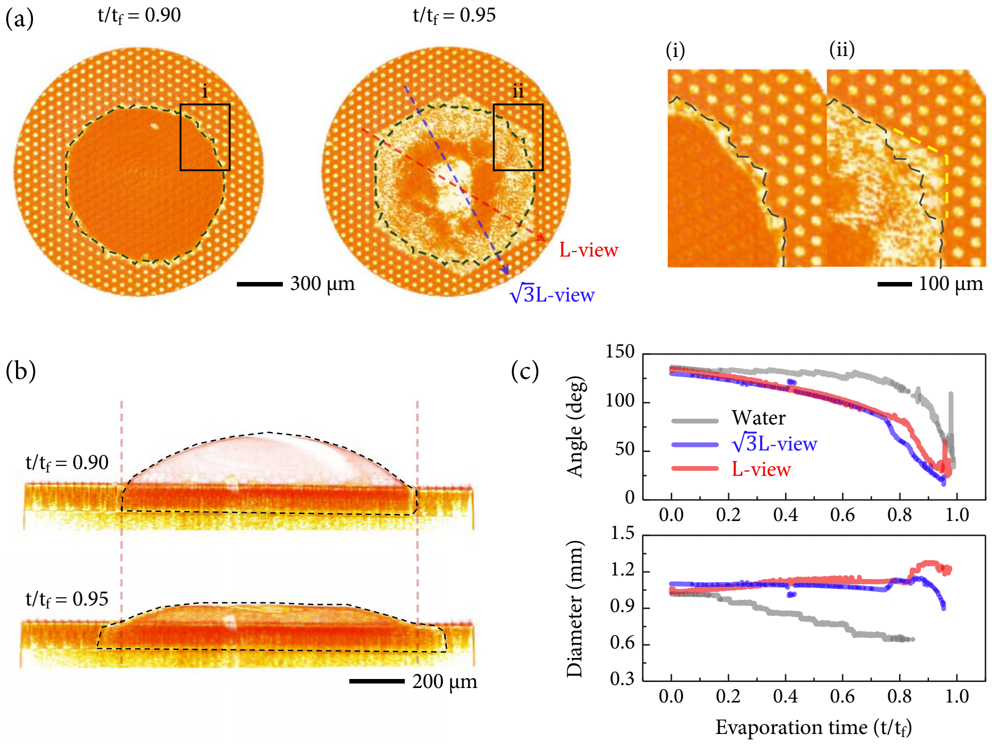

FIG. 3. Evaporation dynamics for hexagonal deposits. (a) Before and after making hexagonal deposits. Sides along $\sqrt{3}L$ direction and points along L direction are formed at $t/t_f \sim 0.95$, as illustrated in up-close images (i) for $t/t_f \sim 0.90$ and (ii) for $t/t_f \sim 0.95$. (b) Corresponding side-view images of (a). Spherical cap shapes remain until $t/t_f \sim 0.90$ and deform at $t/t_f \sim 0.95$ by protrusion into micropillar forests. (c) Global evaporation dynamics for pure (water) and colloidal fluids. Contact angle gradually decreases while diameter is invariant for colloidal fluids, whereas contact diameter gradually decreases while contact angle is invariant for pure fluids. This discrepancy suggests that colloidal particles would significantly dominate evaporation dynamics of colloidal fluids.

turn into hexagonal bottoms at $t/t_f \sim 0.95$ [Fig. 3(a)]. Interestingly, hexagonal sides and points appear along the L direction (where L is the nearest-neighbor interpillar distance) and the $\sqrt{3}L$ direction (where $\sqrt{3}L$ is the nearest-neighbor interpillar distance), respectively. Here each $\sqrt{3}L$-view and L-view images are identical, indicating isotropy of hexagonal deposits. In addition, the circular bottom shape [Fig. 3(a)] and the spherical cap shape [Fig. 3(b)] remain until $t/t_f \sim 0.90$, implying that the evaporation dynamics at $t/t_f < 0.90$ for hexagonal deposits would be governed by the spherical cap evaporation model.

We compare the evaporation dynamics for pure and colloidal fluids on micropillar arrays by measuring droplet contact angle and diameter, as summarized in Fig. 3(c). For colloidal fluids, contact angle gradually decreases with time while contact diameter remains invariant until $t/t_f \sim 0.70$, indicating a constant contact radius mode. Inversely, for water droplets, contact diameter continually decreases with time while contact angle is almost constant until $t/t_f \sim 0.70$, indicating a constant contact angle mode. The difference in evaporation dynamics between pure and colloidal fluids is due to the addition of colloidal particles. As expected, colloidal particles contribute to self-pinning of contact line [4]. After gradual ($0 < t/t_f < 0.70$) and rapid ($0.70 < t/t_f < 0.95$) decreases in contact angles for colloidal fluids, the spherical cap volume is shrunk and permeated into micropillar forests at $t/t_f > 0.95$ [Fig. 3(b)]. Abrupt increases in contact angles

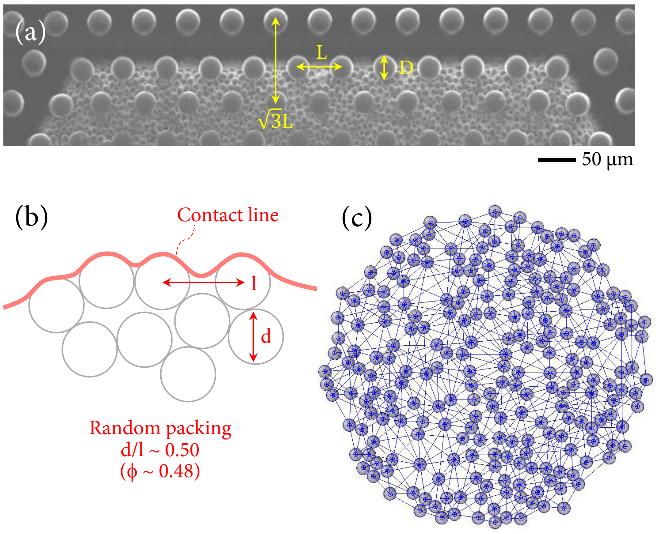

FIG. 4. Random packing of colloids. (a) A up-close SEM image for hexagonal deposits ($L = 60$ μm, $D = 30$ μm, $d = 10$ μm) demonstrates random packing of colloids. (b) A schematic illustration of random packing suggests that colloidal particles would contribute to local contact line pinning. (c) An example 2D image of random packing with silica colloids immersed into water, selected from a full 3D x-ray tomography image, shows $d/l \sim 0.50$ for $\phi \sim 0.48$, as consistent with [39]. The lines in (c) demonstrate a network to connect centers of spheres.

appear at $t/t_f > 0.95$ in both pure and colloidal fluids [Fig. 3(c)]. Interestingly, hexagonal sides and points evolve after $t/t_f \sim 0.95$. The x-ray microscopic observations suggest that the presence of colloidal particles would be helpful to facilitate hexagonal deposits.

C. Random packing of colloids

Colloidal particles that become packed between micropillar arrays would be favorable to facilitate hexagonal deposits. Here, the particle packing fraction (ϕ) would reach random packing [38], as shown in a up-close SEM image for hexagonal deposits in Fig. 4(a). The pillar density, D/L, is defined from micropillar arrays and measured as $D/L \sim 0.50$ in Fig. 4(a). Similarly, the particle density, d/l, for colloidal particles is determined from mean center-to-center distance (l) and particle diameter (d) as illustrated in Fig. 4(b). We measure the particle density as $d/l \sim 0.50$ for $\phi \sim 0.48$ with x-ray tomography from an example random packing with silica colloids in Fig. 4(c). This result agrees well with the previous measurement of mean particle-to-particle distance (m) as $1.2d$ for $\phi \sim 0.44$ [39], resulting in $d/l \sim 0.45$ because $m = l + d$. Presumably, colloidal particles immersed with water are randomly packed inside hexagonal deposits during droplet evaporation.

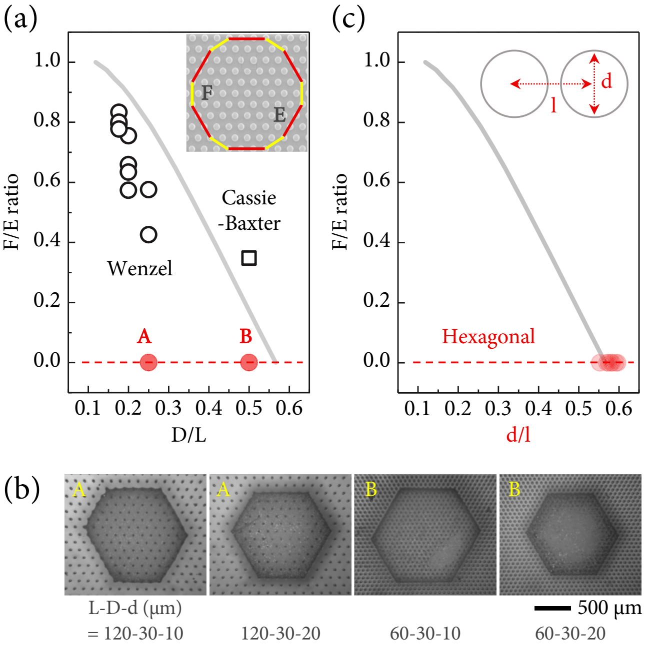

FIG. 5. Local contact line pinning by colloids. (a) The ratio of dodecagon side lengths, F/E, of colloidal deposits versus the pillar density, D/L, of hexagonal arrays, indicating dodecagonal droplets at $F/E = 1$ and hexagonal droplets at $F/E = 0$. The previous prediction from pure fluids (the solid line) [19] does not explain our experiments for hexagonal deposits (A and B conditions) at $F/E = 0$. The open circles and the open squares represent the Wenzel deposits and the Cassie-Baxter deposits, respectively, which appear at four D/L conditions, while the hexagonal deposits appear only at two D/L conditions. (b) Hexagonal deposits reproduced from seven different *L-D-d* conditions, as demonstrated by digital microscopic images. (c) All data for hexagonal deposits are collapsed to the particle density, $d/l = 0.54$–0.58, which intercepts the hexagonal condition at $F/E = 0$ [19]. The Wenzel and the Cassie-Baxter deposits are irrelevant to the polygonal conditions, because they are spherical as shown in Fig. 2. This result suggests that colloidal particles would predominately control local contact line pinning to facilitate hexagonal deposits.

D. Local contact line pinning

We consider the mechanism for polygonal droplet shape control with pure fluids on micropillar arrays [19]. To achieve polygonal droplets, the pillar density, D/L, is a critical parameter because it determines the ratio of dodecagon side lengths, F/E, where $F/E = 0$ corresponds to hexagonal droplets [19]. In Fig. 5(a), all data for colloidal deposits show disagreement with the previous expectation (solid line) taken for polygonal droplets of pure fluids [19]. The initial droplet volume and the initial colloid volume fraction are controlled as 2.0 ± 0.2 μl and 2.5 ± 0.1 vol.%, respectively. Particularly, hexagonal deposits at $F/E = 0$ are found at $D/L \sim 0.25$ (A condition) as well as $D/L \sim 0.50$ (B condition), which are impossible for pure fluids [19]. We reproduce seven examples of hexagonal deposits at A and B conditions, as shown in Fig. 5(b). This result implies that the mechanism of hexagonal deposits is regardless of the pillar density. Instead, we apply the particle density, d/l, to Fig. 5(c) and find an excellent agreement with experiments. All d/l data taken from SEM images after evaporation are collapsed to $d/l = 0.54$–0.58 at $F/E = 0$ that corresponds to isotropic hexagonal deposits. Here the comparable size of particles to pillars is favorable to reproduce hexagonal deposits, which are obtainable at

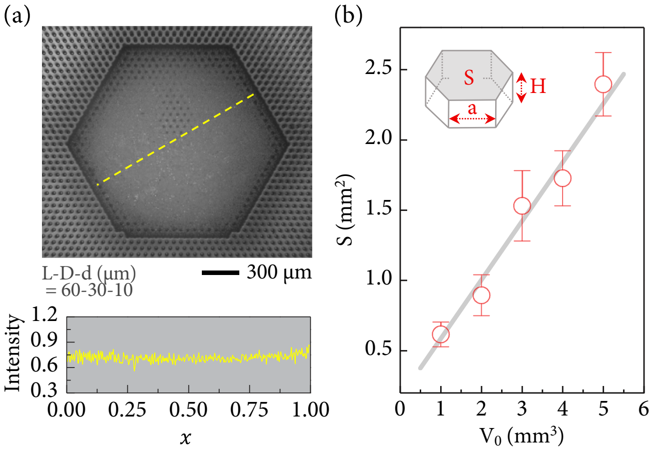

FIG. 6. Hexagonal prism model. (a) The hexagonal deposit, taken by a digital microscope, shows the quite uniform deposition, as supported by the deposition profile (below), taken from the inverted gray scale along the dashed line. (b) The surface area of the base S is predictable, based on the hexagonal prism model with the height H and the base edge a (as illustrated). In experiments, S is proportional to the initial droplet volume V_0, as consistent with the theoretical prediction from $S = (\phi H)^{-1}\phi_0 V_0$. The slope is 0.42, corresponding to $\phi = 0.6$, $H = 0.1$ mm, $\phi_0 = 0.025$, and $V_0 = 2$ mm^3 for the completely evaporated deposit. The validity of the hexagonal prism model suggests the uniformity in thickness and the controllability of hexagonal deposits.

$D/d = 1.6$–3.0, not at $D/d > 30$ in our experiments. We suppose that colloidal particles would predominately contribute to local contact line pinning that facilitates hexagonal deposits.

E. Hexagonal prism model

The deposition profile is quite uniform and hence a hexagonal prism model is plausible with the height H and the base edge a, as shown in Fig. 6. For the hexagonal prism, the surface area of the base is $S = \frac{3\sqrt{3}}{2}a^2$ and the hexagonal deposit volume is $V = SH$. The deposit volume is controlled by the initial droplet volume V_0, the initial particle volume fraction ϕ_0, and the particle packing fraction ϕ as $V = \phi_0 V_0/\phi$. Consequently, we obtain

$$S = (\phi H)^{-1}\phi_0 V_0. \tag{1}$$

The linear proportion of S with V_0 implies the controllability of the hexagonal shapes.

Finally, we discuss a potential to expand polygonal deposits. For pure fluids, polygonal arrays of microtextured surfaces can be adopted to achieve square, hexagonal, octagonal, and circular-shaped liquid deposit films [19,40–45]. Further study is required by altering micropillar arrays and colloidal fluids to control local contact line pinning for polygonal deposits of colloidal particles.

IV. CONCLUSION

Our study reveals a progress that governs droplet evaporation on micropillar surfaces to produce unifrom colloidal assembly. We demonstrate a versatile method to achieve crack-free uniform hexagonal deposits of colloidal particles through droplet evaporation on micropillar arrays. Colloidal fluids evaporate on hexagonal micropillar arrays and eventually turn into hexagonal deposits. Interestingly, colloidal particles would predominately control self-pinning and local contact line pinning. This study shows a feasibility for high-quality evaporation-driven polygonal deposits of colloidal particles.

ACKNOWLEDGMENTS

This research was supported by Basic Science Research Program through the National Research Foundation of Korea (NRF) funded by the Ministry of Education (Grants No. NRF-2016R1D1A1B01007133 and No. 2019R1A6A1A03033215).

[1] P. J. Lu and D. A. Weitz, Colloidal particles: Crystals, glasses, and gels, Annu. Rev. Condens. Matter Phys. **4**, 217 (2013).

[2] B. J. Gans and U. S. Schubert, Inkjet printing of well-defined polymer dots and arrays, Langmuir **20**, 7789 (2004).

[3] N. A. Fleck, R. M. McMeeking, and T. Kraus, Convective assembly of a particle monolayer, Langmuir **31**, 13655 (2015).

[4] B. M. Weon and J. H. Je, Self-Pinning by Colloids Confined at a Contact Line, Phys. Rev. Lett. **110**, 028303 (2013).

[5] B. M. Weon and J. H. Je, Fingering inside the coffee ring, Phys. Rev. E **87**, 013003 (2013).

[6] J. Park and J. Moon, Control of colloidal particle deposit patterns within picoliter droplets ejected by ink-jet printing, Langmuir **22**, 3506 (2006).

[7] J. L. Garcia-Cordero and Z. H. Fan, Sessile droplets for chemical and biological assays, Lab Chip **17**, 2150 (2017).

[8] D. Quere, Wetting and roughness, Annu. Rev. Mater. Res. **38**, 71 (2008).

[9] D. Bonn, J. Eggers, J. Indekeu, J. Meunier, and E. Rolley, Wetting and spreading, Rev. Mod. Phys. **81**, 739 (2009).

[10] W. Xu, R. Leeladhar, Y. T. Kang, and C. H. Choi, Evaporation kinetics of sessile water droplets on micropillared superhydrophobic surfaces, Langmuir **29**, 6032 (2013).

[11] J. Y. Kim, K. Cho, S. Ryu, S. Y. Kim, and B. M. Weon, Crack formation and prevention in colloidal drops, Sci. Rep. **5**, 13166 (2015).

[12] R. D. Deegan, Pattern formation in drying drops, Phys. Rev. E **61**, 475 (2000).

[13] R. D. Deegan, O. Bakajin, T. F. Dupont, G. Huber, S. R. Nagel, and T. A. Witten, Contact line deposits in an evaporating drop, Phys. Rev. E **62**, 756 (2000).

[14] B. M. Weon and J. H. Je, Capillary force repels coffee-ring effect, Phys. Rev. E **82**, 015305(R) (2010).

[15] P. J. Yunker, T. Still, M. A. Lohr, and A. G. Yodh, Suppression of the coffee-ring effect by shape-dependent capillary interactions, Nature **476**, 308 (2011).

[16] J. Y. Kim and B. M. Weon, Evaporation of strong coffee drops, Appl. Phys. Lett. **113**, 183704 (2018).

[17] S. Y. Lee, H. Kim, S.-H. Kim, and H. A. Stone, Uniform Coating of Self-Assembled Noniridescent Colloidal Nanostructures using the Marangoni Effect and Polymers, Phys. Rev. Appl. **10**, 054003 (2018).

[18] T. Cubaud and M. Fermigier, Faceted drops on heterogeneous surfaces, Europhys. Lett. **55**, 239 (2001).

[19] R. Raj, S. Adera, R. Enright, and E. N. Wang, High-resolution liquid patterns via three-dimensional droplet shape control, Nat. Commun. **5**, 4975 (2014).

[20] A. Kumar and R. Raj, Droplets on microdecorated surfaces: Evolution of the polygonal contact line, Lagmuir **33**, 4854 (2017).

[21] K. Zhao and T. G. Mason, Assembly of colloidal particles in solution, Rep. Prog. Phys. **81**, 126601 (2018).

[22] R. van Dommelen, P. Fanzio, and L. Sasso, Surface self-assembly of colloidal crystals formicro- and nano-patterning, Adv. Colloid Interf. Sci. **251**, 97 (2018).

[23] L. Bansal, P. Seth, B. Murugappan, and S. Basu, Suppression of coffee ring: (Particle) size matters, Appl. Phys. Lett. **112**, 211605 (2018).

[24] L. Bansal, P. Seth, S. Sahoo, R. Mukherjee, and S. Basu, Beyond coffee ring: Anomalous self-assembly in evaporating nanofluid droplet on a sticky biomimetic substrate, Appl. Phys. Lett. **113**, 213701 (2018).

[25] M. Dicuangco, S. Dash, J. A. Weibel, and S. V. Garimella, Effect of superhydrophobic surface morphology on evaporative deposition patterns, Appl. Phys. Lett. **104**, 201604 (2014).

[26] H. Jin, Y. Li, P. Zhang, S. Nie, and N. Gao, The investigation of the wetting behavior on the red rose petal, Appl. Phys. Lett. **108**, 151605 (2016).

[27] M. Lee, W. Kim, S. Lee, S. Baek, K. Yong, and S. Jeon, Water droplet evaporation from sticky superhydrophobic surfaces, Appl. Phys. Lett. **111**, 021603 (2017).

[28] Y. Hu, Y. Zhang, H. Yuan, R. Wang, S. Jiang, Z. Lao, G. Li, D. Wu, J. Li, and J. Chu, Capillary-assisted localized crystallization on discrete micropillar rings, Appl. Phys. Lett. **113**, 251904 (2018).

[29] N. Vogel, M. Retsch, C. A. Fustin, A. D. Campo, and U. Jonas, Advances in colloidal assembly: The design of structure and hierarchy in two and three dimensions, Chem. Rev. **115**, 6265 (2015).

[30] S. H. Kim and G. R. Yi, Colloidal photonic crystals for sensor applications, in *Photonic Materials for Sensing, Biosensing and Display Devices*, edited by M. J. Serpe, Y. Kang, and Q. M. Zhang (Springer, Berlin, 2016), pp. 51–78.

[31] Z. Xu, L. Wang, F. Fang, Y. Fu, and Z. Yin, A review on colloidal self-assembly and their applications, Curr. Nanosci. **12**, 725 (2016).

[32] S. Devineau, M. Anyfantakis, L. Marichal, L. Kiger, M. Morel, S. Rudiuk, and D. Baigl, Protein absorption and reorganization on nanoparticles probed by the coffee-ring effect: Application to single point mutation detection, J. Am. Chem. Soc. **138**, 11623 (2016).

[33] W. G. Bae, M. K. Kwak, H. E. Jeong, C. Pang, H. Jeong, and K. Y. Suh, Fabrication and analysis of enforced dry adhesives with core-shell micropillars, Soft Matter **9**, 1422 (2013).

[34] X. Chen, R. Ma, J. Ki, C. Hao, W. Guo, B. L. Luk, S. C. Li, S. Yao, and Z. Wang, Evaporation of Droplets on Superhydrophobic Surfaces: Surface Roughness and Small Droplet Size Effects, Phys. Rev. Lett. **109**, 116101 (2012).

[35] P. Papadopoulos, L. Mammen, X. Deng, D. Vollmer, and H. J. Butt, How superhydrophobicity breaks down, Proc. Natl. Acad. Sci. USA **110**, 3254 (2013).

[36] C. Antonini, J. B. Lee, T. Maitra, S. Irvine, D. Derome, M. K. Tiwari, J. Carmeliet, and D. Poulikakos, Unraveling wetting transition through surface textures with X-rays: Liquid meniscus penetration phenomena, Sci. Rep. **4**, 4055 (2014).

[37] E. Bormashenko, Progress in understanding wetting transitions on rough surfaces, Adv. Colloid Interf. Sci. **222**, 92 (2015).

[38] H. J. H. Brouwers, Particle-size distribution and packing fraction of geometric random packings, Phys. Rev. E **74**, 031309 (2006).

[39] D. T. Wasan and A. D. Nikolov, Spreading of nanofluids on solids, Nature **423**, 156 (2003).

[40] L. Courbin, J. C. Bird, M. Reyssat, and H. A. Stone, Dynamics of wetting: From inertial spreading to viscous imbibition, J. Phys.: Condens. Matter. **21**, 464127 (2009).

[41] L. Courbin, E. Denieul, E. Dressaire, M. Roper, A. Ajdari, and H. A. Stone, Imbibition by polygonal spreading on microdecorated surfaces, Nat. Mater. **6**, 661 (2007).

[42] M. Sbragaglia, A. M. Peters, C. Pirat, B. M. Borkent, R. G. H. Lammertink, M. Wessling, and D. Lohse, Spontaneous Breakdown of Superhydrophobicity, Phys. Rev. Lett. **99**, 156001 (2007).

[43] S. J. Kim, J. Kim, M. W. Moon, K. R. Lee, and H. Y. Kim, Experimental study of drop spreading on textured superhydrophilic surfaces, Phys. Fluids **25**, 092110 (2013).

[44] V. Hisler, L. Vonna, V. L. Houerou, S. Knopf, C. Gauthier, M. Nardin, and H. Haidara, Model experimental study of scale invariant wetting behaviors in Cassie-Baxter and Wenzel regimes, Langmuir **30**, 9378 (2014).

[45] Q. Yuan, X. Huang, and Y. P. Zhao, Dynamic spreading on pillar-arrayed surfaces: Viscous resistance versus molecular friction, Phys. Fluids **26**, 092104 (2014).